Chemistry–A European Journal

Research Article
doi.org/10.1002/chem.202303762

Chemistry Europe
European Chemical
Societies Publishing

www.chemeurj.org

Probing the Isolobal Relation between Cp'''NiP₃ and White Phosphorus by Experimental Charge Density Analysis

Florian Meurer,[a] Florian Kleemiss,[a, b] Christoph Riesinger,[a] Gábor Balázs,[a] Vedran Vuković,[a, c] Ilya G. Shenderovich,[a] Christian Jelsch,[c] and Michael Bodensteiner*[a]

Dedicated to Professor Nikolaus Korber on the occasion of his 60th birthday.

An in-depth analysis of the description of bonding within Cp'''Ni-*cyclo*-P₃ (Cp''' = 1,2,4-*tri*-tert-butylcyclopentadienyl, [Ni]P₃) employing X-ray diffraction based multipolar modeling, density functional theory (DFT) as well as an "experimental wavefunction" obtained from X-ray restrained wavefunction (XRW) fitting is presented. The results are compared to DFT calculations on white phosphorus – an isolobal analogue to [Ni]P₃. A complementary bonding analysis shows insights into the reactivity of [Ni]P₃. The isolobal principle is reflected in every aspect of our analysis and the employed methods seamlessly predict the differences in reactivity of [Ni]P₃ and P₄. Crystallographic modeling, solid-state NMR, and DFT calculations describe the dynamic behavior of the *cyclo*-P₃ unit in the title molecule.

Introduction

Supporting sophisticated theoretical investigations are now standard in publications in almost every discipline of chemistry. In many cases they are based on previously determined X-ray crystal structures after gas phase geometry optimization. This order shows that there is a tendency to attribute little chemical information content to experimental crystal structure determination. This is astonishing in several respects. On the one hand, it has been shown decades ago that very precise chemical information can be obtained with quantum crystallographic methods.[1–3] On the other hand, X-ray sources and detectors have reached a level of development that offers an immense photon flux and simultaneously, the ability to detect single photons. This allows for such precise, fast experiments that crystal structure determinations nowadays are a matter of

minutes to hours.[4] Finally, it has become feasible to examine two sides of the same medal: both the square of a wavefunction and the Fourier transform of the diffraction pattern provide the electron density distribution.[3] However, the most commonly used independent atom model for crystal structure refinements is a very rough description, which assumes that all atoms of an element in a compound are identical and neutral, with spherically distributed electron density. Moving beyond that simplistic model, hand in hand with theoretical computations of varying degrees of sophistication, allows for obtaining the best of the two worlds: A precise experimental geometry and an appropriately fitted wavefunction.

In this work, we investigate the P–P and Ni–P bonding in [Ni]P₃ (Scheme 1) with complementary bonding analysis of quantum crystallographic models from multipolar refinement as well as an X-ray restrained wavefunction fitting model. The multipolar model (MM) as a parametrized approach to extend the independent atom model (IAM) by spherical harmonical

[a] F. Meurer, Prof. Dr. F. Kleemiss, Dr. C. Riesinger, Dr. G. Balázs, Dr. V. Vuković,
Dr. I. G. Shenderovich, Dr. M. Bodensteiner
Faculty for Chemistry and Pharmacy
University of Regensburg
Universitätsstraße 31, 93053 Regensburg, Germany
E-mail: michael.bodensteiner@ur.de

[b] Prof. Dr. F. Kleemiss
Institute for Inorganic Chemistry
RWTH Aachen
Landoltweg 1a, 52074 Aachen, Germany

[c] Dr. V. Vuković, Dr. C. Jelsch
Cristallographie, Résonance Magnétique et Modélisations CNRS, UMR 7036,
Institut Jean Barriol, CNRS and Université de Lorraine BP 70239
F54506 Vandoeuvre-lès-Nancy CEDEX, France

Supporting information for this article is available on the WWW under
https://doi.org/10.1002/chem.202303762
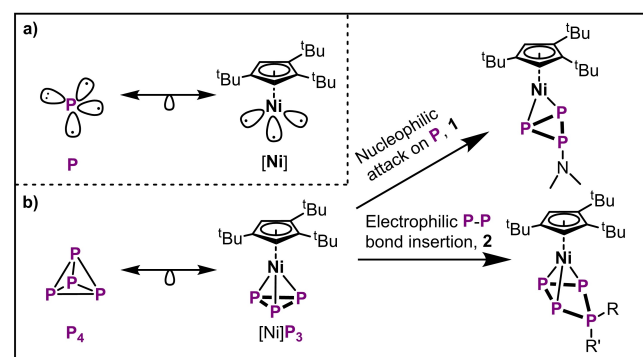
Scheme 1. Isolobal relationships between a phosphorus atom of white phosphorus and the [Ni] fragment (a) or [Ni]P₃ (b) with selected reactivities of [Ni]P₃ shown. **1**: LiNMe₂ in THF at room temperature;[5] **2**: selected scope as in reference.[6]

Chemistry–A European Journal

Research Article
doi.org/10.1002/chem.202303762

Chemistry
Europe
European Chemical
Societies Publishing

terms, closely resembling atomic orbitals, has a long history in the description of the electron density within crystals.[7,8] However, the modelling of transition metal compounds has proved to be especially challenging. In contrast, X-ray restrained wavefuncions (XRWs) yield an "experimental wavefunction" which can be used to describe a molecule or compound beyond topological analysis.[2,3,9]

We compare these findings to theoretical calculations on [Ni]P$_3$ (see Figure 1) and white phosphorus – an isolobal analogue.[10] In this context, we describe the electronic structure of the *cyclo*-P$_3$ fragment, which can be either seen as a planar ligand coordinating to the transition metal or with separate phosphorus atoms bound individually.

Results and Discussion

Experimental and Methods

A high-resolution ($d_{min} = 0.54$ Å) X-ray diffraction data set using Mo K_α radiation of a [Ni]P$_3$ single crystal serves as the basis for the crystallographic studies. Multipolar modeling according to the Hansen & Coppens formalism was performed within the *MoPro* software with the refinement of multipolar parameters as described in the supporting information.[11,12,13] Anisotropic displacement parameters for hydrogen atoms were obtained using the *SHADE3* server.[14] *VMoPro* and *MoProViewer* modules were used to perform the topological analysis. Further information can be found in the supporting information.

A Hirshfeld-Atom Refinement (HAR) yielded the starting geometry for the XRW fitting in the *TONTO* quantum crystallographic software suite.[15–17] HAR uses the geometry of the (IAM) for a wavefunction calculation and partitions the wavefunction's corresponding electron density into non-spherical atomic formfactors. These formfactors were then used in the crystallographic refinement of atomic positions and displacement
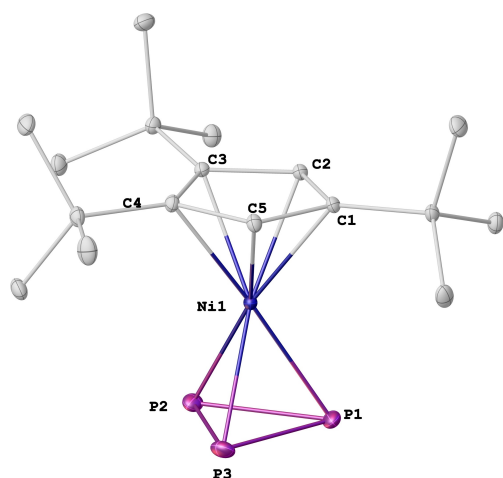
parameters. HAR was performed following this procedure iteratively until a given convergence criterium was met.

HAR was performed using *ORCA5* (M062X/def2-TZVP) and the resulting wavefunction yielded non-spherical atomic form factors for all atoms (including hydrogens) in [Ni]P$_3$ using a Hirshfeld partitioning scheme. This calculation was performed by *NoSpherA2* in the *Olex2* crystallographic suite.[18–22] A procedure of wavefunction generation, partitioning, and refinement was repeated until convergence was achieved. The resulting geometry from HAR was then used as the geometry for the XRW fitting. Contrary to HAR, the XRW fitting is perturbed during the self-consistent-field (SCF) procedure by weighted Lagrange multiplication with the agreement between measured and calculated structure factors defined as follows:

$$J(\Psi) = E(\Psi) + \lambda(\chi^2(\Psi) - \Delta) \tag{1}$$

where the Jayatilaka functional J (Eq. 1) consists of the (single-point) energy E of the wavefunction Ψ modified with the λ-weighted perturbation term χ^2 and with Δ as the desired agreement for this term. In our specific case, Δ was set to zero in order to extract the maximum possible information from the diffraction data. χ^2 (Eq. 2) represents the weighted differences between the calculated and measured structure factors ($F^{calc/obs}$) from the Bragg intensities as follows:

$$\chi^2(\Psi) = \frac{1}{N_{refl} - N_{par}} \sum_{i=1}^{N_{refl}} \frac{\xi \left|F_i^{calc}(\Psi)\right|^2 - \left|F_i^{obs}\right|^2}{(\sigma_i^{obs})^2} \tag{2}$$

where $N_{refl/par}$ are the number of reflections and parameters (N_{par} is traditionally set to one in XRW determinations, the parameter being λ), ξ is a scaling factor, and σ is the uncertainty of the measured structure factors. This assumes that purely statistical weighting schemes are used throughout the procedure.

During the XRW fitting procedure, the geometry from HAR was used to perform a wavefunction calculation using the (spin-orbital restricted) Hartree-Fock (HF) method using the def2-TZVP basis set. The λ parameter was initially set to zero to yield a pure HF calculation of the solid-state [Ni]P$_3$ geometry obtained from HAR. λ was then incrementally increased by steps of 0.01 to increase the influence of the measured structure factors. This procedure was repeated until a maximum perturbation with the corresponding value of λ was achieved while the SCF still converged. This convergence is shown in the supporting information. The resulting wavefunction was then used to generate non-spherical atomic form factors according to Hirshfeld stockholder-partitioning.[21]

This way, we started with a model based on *ab-initio* calculated wavefunction and extracted the remaining influences on the electron density, which were not accounted for in HF, such as electron correlation and polarization, from the experimental electron density. A comprehensive overview and discussion on extracting these properties can be found in references [23, 24].

X-ray diffraction data were collected using Mo K_α (wavelength = 0.71073 Å) as well as Cu K_β (wavelength = 1.39222 Å)

Figure 1. Structure and labelling scheme for selected atoms of [Ni]P$_3$. Hydrogen atoms are omitted for clarity, ellipsoids are drawn at the 50% probability level (Mo K_α HAR model).

Chemistry–A European Journal

Research Article
doi.org/10.1002/chem.202303762

Chemistry Europe
European Chemical
Societies Publishing

radiation to compare the results obtained using these different data sets for both XRW fitting and multipolar modelling. From the results of this comparison, which can be found in detail in the supporting information, we chose the Mo-XRW model with a λ parameter of 0.42 as the best result to investigate the bonding situation in $[Ni]P_3$ without overfitting due to the introduction of experimental noise and errors into the data. Mo-XRW was then compared to the multipolar model (MM) of Mo K_α data for the topological analysis, while all other bonding indices were extracted from the wavefunction analysis. These characteristics for $[Ni]P_3$ were also compared to the DFT optimized geometry of P_4 (M062X/def2-TZVP) or to its normal-mode corrected solid-state structure (XRD).[25]

In this work, we report to the best of our knowledge on the first multipolar model as well as XRW fitting procedure using Cu K_β radiation. The main differences between Mo K_α and Cu K_β radiation lie in the maximum achievable resolution, raw intensity, and peak-splitting. While Mo K_α provides much higher resolution data sets (d_{min}(Mo K_α) = 0.355 Å, d_{min}(Cu K_β) = 0.696 Å), Cu K_β gives higher intensity and does not observably exhibit the peak-splitting common to all K_α radiation types. For both charge density modelling approaches we found reasonable results even with the lower resolved Cu K_β data set. In particular, the topological analysis of the multipolar model and wavefunction-based bonding analysis closely resembled the descriptions achieved with Mo K_α radiation, despite the additional challenge associated with using Cu K_β radiation with a nickel compound. Nickel has its K shell absorption edge a slightly lower in energy than Cu K_β radiation, so it has a particularly high elemental absorption for nickel. More comprehensive crystallographic details regarding this effort can be found in the supporting information.

Geometry

White phosphorus exhibits T_d symmetry in the gas phase with six equidistant, chemically equivalent P–P bonds. P_4 is notoriously difficult to crystallize in a manner suitable for high quality diffraction data, so our results besides the geometry are compared with DFT calculations. The NiP_3 fragment in $[Ni]P_3$ shows a tetrahedral geometry, which is distorted by the [Ni] fragment and shows different interatomic distances and bond angles. The geometry of the molecule in the gas phase differs only slightly from the one in the crystalline phase which can be attributed to the weak intermolecular interactions in the crystalline phase.[26]

The P–P distances in $[Ni]P_3$ are significantly shorter than in white phosphorus despite the similar ring strain (see Table 1). This might indicate stronger bonds between the phosphorus atoms in $[Ni]P_3$ compared to P_4. In contrast, the Ni–P bonds are generally longer than the P–P bonds. While the bond angles between the phosphorus atoms are comparable to those in P_4, the P–Ni–P bond angles differ strongly and are smaller in $[Ni]P_3$. Thus, the tetrahedral geometry in P_4 is distorted by the isolobal substitution of a phosphorus atom by the [Ni] fragment.

Topological Analysis

Table 2 shows the selected topological properties of the different models according to Bader's quantum theory of atoms in molecules (QTAIM). This method analyses chemical bonding by following the topology of the total electron density distribution in real space.[27,28]

There is generally less electron density at the bond critical points (BCP) between Ni and phosphorus than between two phosphorus atoms (see Table 2). The Laplacian values at the bond critical points also indicate a Valence Shell Charge Concentration (VSCC, i.e., negative Laplacian values) at the BCPs between two phosphorus atoms and a Valence Shell Charge Depletion (VSCD, i.e., positive Laplacian values) in all Ni–P bonds. The values of the electron density at the BCP are considerably high in comparison with other literature known transition metal-phosphorus bonds.[29,30,31] The positive Laplacians at the BCP indicate intermediate dative bonds.

A closer look at the distribution of the Laplacian of the electron density along the topological bond paths shows symmetrical P–P bonds with a negative Laplacian plateau at the BCPs and similar progression between the MM and XRW models. The plateau stays in the negative regime for the XRW and MM model, as expected for covalent non-polarized bonds.[32] A value closer to zero is consistent with a systematic comparison of the XRW method with MM by Woinska et al.[24]

This study on organic compounds found the Laplacian values overestimated in the MM compared to the XRW method, which itself is consistent with the DFT calculation of P_4. So far, the differences between XRW and MM in transition-metal complexes have not been systematically studied, but our findings suggest a similar behavior in this case.

Table 1. Selected distances and angles in the different models of P_4 and $[Ni]P_3$. Note that HAR and XRW geometries are identical.

	P_4		$[Ni]P_3$		
	XRD[25]	DFT	DFT	MM (Mo K_α)	HAR (Mo K_α)
P–P distances/Å	2.201 (2)–2.209 (1)	2.2031	P1–P2: 2.1549 P1–P3: 2.1550 P2–P3: 2.1558	P1–P2: 2.1481(3) P1–P3: 2.1446(2) P2–P3: 2.1534(3)	P1–P2: 2.1465(1) P1–P3: 2.1432(1) P2–P3: 2.1508(2)
Ni–P distances/Å	–	–	Ni–P1: 2.2670 Ni–P2: 2.2660 Ni–P3: 2.2970	Ni–P1: 2.2471(2) Ni–P2: 2.2376(2) Ni–P3: 2.2477(2)	Ni–P1: 2.2460(1) Ni–P2: 2.2370(1) Ni–P3: 2.2467(1)
P–P–P Angles/°	59.74 (2)–60.39 (2)	60.00	59.98–60.03	59.810(13)–60.217(13)	59.984(4)–60.185(4)

Chemistry–A European Journal

Research Article
doi.org/10.1002/chem.202303762

Chemistry Europe
European Chemical
Societies Publishing

Table 2. Values of electron density (ρ) and Laplacian of the electron density ($\nabla^2(\rho)$) at selected bond critical points according to the QTAIM for the different models of [Ni]P$_3$. The DFT model of P$_4$ DFT model is added for comparison.

Atom1	Atom2	DFT		MM (Mo K_α)		XRW (Mo K_α)	
		$\rho/e\cdot\text{Å}^{-3}$	$\nabla^2(\rho)/e\cdot\text{Å}^{-5}$	$\rho/e\cdot\text{Å}^{-3}$	$\nabla^2(\rho)/e\cdot\text{Å}^{-5}$	$\rho/e\cdot\text{Å}^{-3}$	$\nabla^2(\rho)/e\cdot\text{Å}^{-5}$
Ni	P1	0.560	1.844	0.557(6)	3.61(8)	0.596	1.706
Ni	P2	0.562	1.836	0.577(5)	3.72(7)	0.608	1.507
Ni	P3	0.558	1.894	0.536(8)	3.70(9)	0.563	1.804
P1	P2	0.788	−2.418	0.760(5)	−0.3(1)	0.816	−2.514
P1	P3	0.788	−2.430	0.749(5)	−0.22(8)	0.808	−2.690
P2	P3	0.787	−2.411	0.756(6)	−0.20(9)	0.810	−2.595
P(P$_4$)	P(P$_4$)	0.202	−1.344	–	–	–	–

The Ni–P bonds exhibit highly asymmetrical Laplacians of the electron density along bonding paths in every model – indicative of a dative bonding character. There are pronounced VSCCs between the BCPs and phosphorus atoms, but strong depletions of electron density towards the nickel center. This indicates highly polarized Ni–P bonds which are expected from the differences in electronegativity. Again, a higher Laplacian at the BCP is observed in the MM than in the XRW and DFT calculation of [Ni]P$_3$.

The 2D maps of the Laplacian in the *cyclo*-P$_3$ (see Figure 2) plane indicate a strong smearing of electron density in the P–P bonds in the XRW model with a larger overlap of electron density accumulation areas in the vicinity of the bond paths. This smearing was less pronounced in the MM, but generally followed this trend of the 2D Laplacian map of *cyclo*-P$_3$. The

models closely resembled the Laplacian 2D map obtained for the *cyclo*-P$_3$ plane in white phosphorus.

The atomic charges (see Table 3) were consistent with a positively charged nickel and negatively charged phosphorus atoms. Here, the MM showed a similar positive charge for nickel and a more negative charge on the *cyclo*-P$_3$ unit compared to the XRW model.

Generally, the topology of electron density within the Ni–P$_2$ rings allowed for a good comparison with the work by Macchi *et al.* to describe the bonding in terms of the Dewar-Chatt-Duncanson metal-olefine vs. metallacyclopropane model.[8,33] The topology of this system in [Ni]P$_3$ (see Figure S8) was similar to the one that has been described for Ni(COD)$_2$: a σ-donation by the P–P bonds to nickel as well as π-back-bonding, indicated by "inwardly curved, but well separated" Ni–P bond paths has been also described in this study. This pushes the Ni–P$_2$ more to the metallacycle side – despite the positive Laplacian of electron density at the BCP, which is quite small compared to other literature examples.[34] Back-bonding by the metal center was also supported by lower occupancies (see Table S5 in the supporting information) in the *d(xy)* and *d(yz)* orbitals – again similar to the case described by Macchi *et al.*[8] Therefore, the NiP$_3$ fragment could be described close to a *metallatetrahedrane* analogue.

Bonding Indices

Table 4 shows the bonding indices and parameters of [Ni]P$_3$ compared to P$_4$. NBO[35] analysis revealed bonding indices near unity for P–P bonds with a stronger bond between P1 and P3
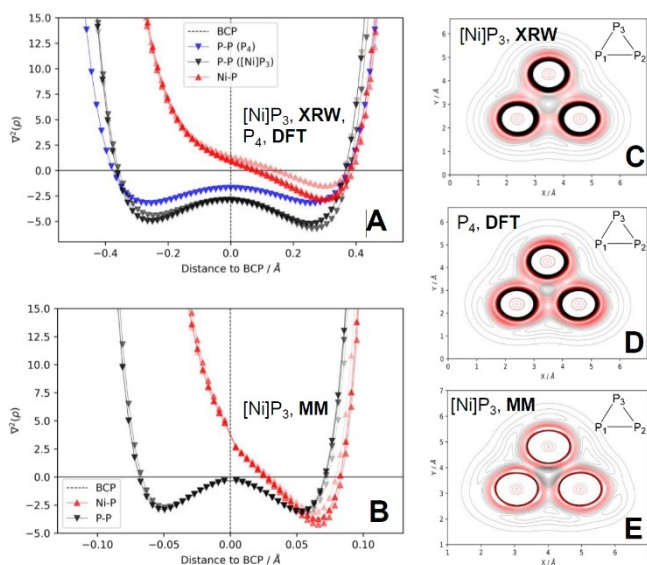
Figure 2. Values for the Laplacian of the electron density along bond critical paths between P–P (black:XRD, blue:DFT, upright triangle: P–P bonds, inverted triangles: Ni–P bonds) and Ni–P (red) in the MM and XRW model (A, B) as well as 2D Laplacian maps of the *cyclo*-P$_3$ fragment with 0.2 eÅ^{-5} iso-lines for the *cyclo*-P$_3$ fragment (C, D, E). In the 2D Laplacian maps, red color indicates a negative, black a positive Laplacian value attributed to valence charge accumulation or depletion, respectively.

Table 3. Bader charges in electrons for selected atoms in each model for [Ni]P$_3$ and P$_4$.

	DFT	MM	XRW
Ni	0.397	0.46(2)	0.416
P1	−0.077	−0.26(2)	−0.133
P2	−0.078	−0.32(2)	−0.065
P3	−0.077	−0.30(3)	−0.132
P (P$_4$)	0.000	–	–

Chemistry–A European Journal

Research Article
doi.org/10.1002/chem.202303762

Chemistry Europe
European Chemical
Societies Publishing

Table 4. Selected bonding indices for the XRW [Ni]P$_3$ model and P$_4$. B. O.: bonding order, WBI: Wiberg bond index, NLMO: natural localized molecular orbitals, Cov: covalent, D. I.: delocalization index.

Atom1	Atom2	NBO				Roby-Gould			
		B.O.	WBI	NLMO*	% Cov	D.I.	Cov. Ind	Ion. Ind	% Cov
Ni1	P1	0.4779	0.4899	0.5583	69.8	0.79	0.45	0.23	79.53
Ni1	P2	0.5338	0.5338	0.8932	77.9	0.81	0.48	0.21	83.23
Ni1	P3	0.5249	0.5071	0.8633	68.0	0.78	0.45	0.25	76.62
P1	P2	0.9987	1.1192	1.1852	98.3	1.20	1.22	0.00	99.1
P1	P3	1.1626	1.1406	1.2408	99.0	1.23	1.26	0.02	99.98
P2	P3	0.9895	1.1100	1.1713	99.1	1.20	1.22	0.02	99.12
P(P$_4$)	P(P$_4$)	1.000	1.0149	1.036	100	1.48	1.00	0.00	100

and slightly weaker bonds of both atoms to P2. This was consistent with the topological analysis of the XRW model, where less negative charge was assigned to P2. In contrast, all Ni–P bonds had a bond order close to 0.5. This value for a metal-heteroatom bond is relatively large in comparison to Ni–C bonding orders of 0.02–0.01. We observed a high occupancy (0.64 e) of the Ni–P anti-bonding orbital, which is mainly of Ni-d and P-p orbital character. The second order perturbation theory revealed a strong contribution of the P-lone-pairs (164 and 160 kJ/mol) for the Ni–P anti-bonding combination with no significant Ni-lone-pair contributions. Besides this, a strong contribution of the Cp''' ligand's "lone-pairs" to the Ni–P anti-bonding was found.

The Wiberg bond index (WBI) following an NPA analysis showed a P–P bond order slightly above unity with about 1.1 electron pairs for each P–P bond. Again, Ni–P bonds possessed about one electron per Ni–P bond. According to the NBO theory, the P–P bonds are expected to be covalent and on average slightly stronger than P–P bonds in white phosphorus. In the natural resonance theory (NRT), the Ni–P bonds exhibited a covalency of about 70%, i.e., of primarily dative covalent character, despite the large difference in electronegativity. NRT described the bonding of *cyclo*-P$_3$ to [Ni] as a mixture of two covalent interactions on average shared across the three centers. For the Lewis picture of [Ni]P$_3$, the dominant resonance

structures (combined 50% weight) exhibited two out of three possible Ni–P bonds (to P1 and P3), and three P–P bonds. This was accompanied by four lone pairs of electrons attributed to the nickel atom, as well as 3.5 lone pairs shared over the *cyclo*-P$_3$ unit. The remaining half lone pair was attributed half to P2, one third to Ni, and the rest shared between the other phosphorus atoms. This suggested that the *cyclo*-P$_3$ provided about three electrons for chemical bonding with the [Ni] fragment. NLMO/NPA bond orders were at 2.31 for Ni excluding Ni–C bonds (3.38 including them), 2.77 for P2 and 3.17 and 3.19 for P1 and P3, respectively.

The P–P bonds in the DFT model of P$_4$ exhibited stronger delocalization than the P–P bonds in [Ni]P$_3$ and a very low delocalization index was calculated for Ni–P bonds. This is also borne out by the Roby-Gould bonding indices. Here, the P–P bond in [Ni]P$_3$ was even stronger compared to the one in P$_4$. A higher covalent character was assumed for the Ni–P bonds according to the Roby-Gould index compared to NBO analysis.

A comparison of the same-spin electron localizability indicator (ELI-D) of P$_4$ and [Ni]P$_3$ in Figure 4 showed a strong similarity in what can be attributed to phosphorus lone pairs. Except for the [Ni] fragment, the *cyclo*-P$_3$ fragment matched the shape of the lone pairs in white phosphorus precisely.

A deeper look into the bonding analysis and integration of charges in the Raub-Jansen scheme following the evaluation of

HOMO   **LUMO**

front   side   front   side
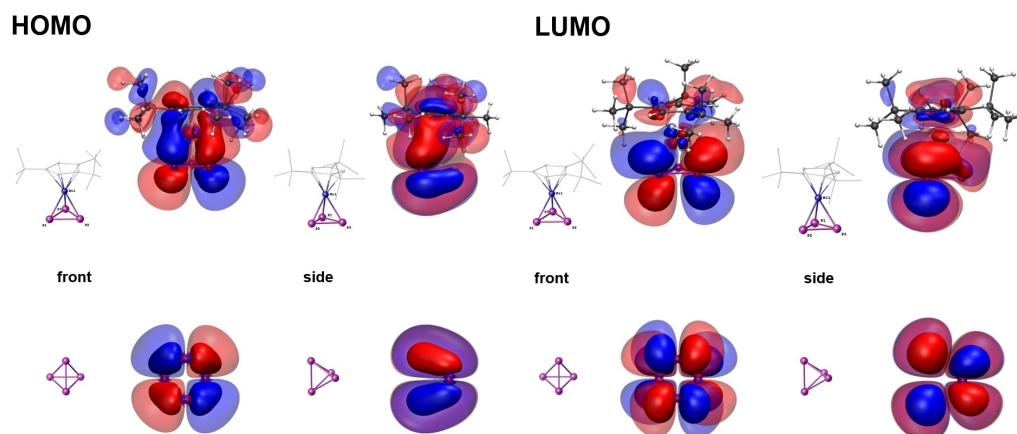
Figure 3. Frontier orbitals of the XRW (Mo K_α) model of [Ni]P$_3$ (upper half) compared to the DFT calculation of P$_4$ (lower half).

Chemistry–A European Journal

Research Article
doi.org/10.1002/chem.202303762
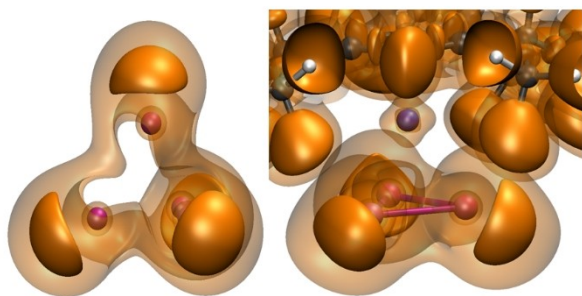
Chemistry Europe
European Chemical
Societies Publishing

Figure 4. Comparison of ELI-D of white phosphorus (left) and [Ni]P$_3$ (right) at iso-surfaces of 1.2 (opaque) and 1.7 e/Å^3 (transparent).

the ELI-D distribution was not possible, since the basins were truncated in an unreproducible way, most likely due to extremely subtle details, that could not be resolved with affordable computational effort. We attributed this to the highly delocalized electronic system in both P$_4$ and [Ni]P$_3$.

Figure 3 shows the XRW model frontier orbitals of [Ni]P$_3$ compared to the frontier orbitals of P$_4$. When reduced to the NiP$_3$ tetrahedron, a similar shape with two nodal planes was observed for the highest occupied molecular orbital. P$_4$ exhibited lobes of this molecular orbital primarily above and below each phosphorus atom, stretching in the bonding direction. In [Ni]P$_3$ a similar behavior was observed for two of the three phosphorus atoms (P1 and P2) with lobes away and towards the [Ni] fragment but stretched in the direction of P3. A similar shape but with an additional nodal plane was observed for the lowest unoccupied molecular orbital of P$_4$. In [Ni]P$_3$, a similar pattern was observed around P1 and P2, with a different, less pronounced contribution of the [Ni] fragment. This suggested that P1 and P2 formed the chemical center for both nucleophilic and electrophilic reactions. This did not fully match the description of Mädl *et al.*, who did not find any significant contribution at these two atoms, but rather at their bonds towards the third phosphorus atom.[5] The resulting LUMO, however, matched their description and was thus also in accord with their observed reactivity towards main-group nucleophiles. Our updated view of the highest occupied molecular orbital was consistent with successful electrophilic insertion into P–P bonds as reported.[6] An overall higher inertness towards air in comparison to white phosphorus could be explained through generally stronger P–P bonds in [Ni]P$_3$ and by hindrance from the sterically demanding [Ni] isolobal replacement.

ing isotropic chemical shifts. The three phosphorus atoms of the *cyclo*-P$_3$ fragment were not chemically equivalent, and therefore, their chemical shift tensors were slightly different. The $^1J(^{31}P^{31}P)$ scalar couplings between them were about 400 Hz, leading to non-first-order NMR spectra. They are also affected by homonuclear ^{31}P–^{31}P dipolar interactions. Nevertheless, the experimental values of the principal components δ_{11}, δ_{22}, and δ_{33} of the chemical shift tensors and the isotropic chemical shifts δ_{iso} could be roughly estimated (see Table 5). Tables S12 and S13 (SI) report the ^{31}P NMR shielding tensors of [Ni]P$_3$ and $^1J(^{31}P^{31}P)$ couplings calculated using the ωB97XD/def2-QZVP approximation. A reference ^{31}P NMR absolute chemical shielding σ^{ref} is required to convert between the chemical shift scale δ used in experiments and the absolute shielding scale σ used in theoretical calculations. With a high degree of accuracy, $\delta \approx \sigma^{ref} - \sigma$. The value of σ^{ref} depends on the approximation used for the calculations and is available elsewhere.[36] For the ωB97XD/def2-QZVP approximation, $\sigma^{ref} = 300$ ppm. The calculated values of the shieldings σ_{iso}, σ_{11}, σ_{22}, and δ_{33} of the three phosphorus nuclei of the *cyclo*-P$_3$ fragment are given in Table S12.

The difference between the experimental and calculated values of δ_{iso} was significant and exceeded the expected margin of error.[36] This difference was most likely due to the influence of the crystal field, which cannot be accounted for in conventional calculation approaches.[37] The difference between the experimental and calculated values of the principal components of the tensors was even larger, but it had two characteristic features. First, the experimental tensor was axially symmetric ($\delta_{11}^{exp} = \delta_{22}^{exp}$), while the calculated tensors were not. Second, the anisotropy of the experimental tensor was smaller than that of the calculated tensors, $|\delta_{11}^{exp}| < |\delta_{11}^{calc}|$ and $|\delta_{33}^{exp}| < |\delta_{33}^{calc}|$. Such features are typical of molecular systems undergoing dynamic changes that are fast on the NMR time scale of microseconds.[38] The δ_{11} and δ_{22} components lay roughly in the plane of the *cyclo*-P$_3$ fragment, and the direction of the δ_{33} component roughly coincided with the normal to this plane. An intermittent rotation of this fragment about this normal led to an axially symmetric tensor with $\delta_{11}^{rot} = \delta_{22}^{rot} = (\delta_{11}^{calc} + \delta_{22}^{calc})/2$. Since the directions of the tensor components did not exactly coincide with the plane of the fragment and the normal, this equality was approximately satisfied, and the rotation also changed the observed value of the δ_{33} component, so that $|\delta_{33}^{rot}| < |\delta_{33}^{calc}|$. Figure S19 in the SI shows the resulting relaxed geometry energies for a 120° rotation of the *cyclo*-P3 fragment perpendicular to the axis connecting the centers of mass of the two cyclic fragments. The activation

Dynamical Behaviour of the cyclo-P$_3$ Fragment

The dynamic behavior of the *cyclo*-P$_3$ fragment was investigated by solid-state ^{31}P NMR spectroscopy. The experimental static and magic angle spinning spectra of [Ni]P$_3$ are shown in Figure S18 in the supporting information. It was difficult to determine from these spectra the exact values of the principal components of the chemical shift tensors and the correspond-

Table 5. Experimental and calculated values of δ_{iso}, δ_{11}, δ_{22}, and δ_{33} of the *cyclo*-P$_3$ fragment.

Nucleus	δ_{iso}/ppm	δ_{11}/ppm	δ_{22}/ppm	δ_{33}/ppm
Experiment	−164	10	10	−520
P1	−190	100	−49	−623
P2	−185	85	−43	−596
P3	−184	128	−49	−632

Chemistry–A European Journal

Research Article
doi.org/10.1002/chem.202303762

Chemistry Europe
European Chemical
Societies Publishing

barrier was only 8.9 kJ/mol, indicating dynamic exchange of the three phosphorus positions.

Conclusions

In summary, we have extensively characterized [Ni]P$_3$ using the most sophisticated methods of experimentally driven charge density analysis. A rare example of a successful X-ray restrained wavefunction fitting of a transition metal complex has provided deep insight into the chemical nature (Scheme 1) of [Ni]P$_3$ – an isolobal analogue of white phosphorus with promise as a phosphorus source with rich reactivity.

Our studies showed a reasonable applicability of Hoffman's isolobal principle when [Ni]P$_3$ is compared to white phosphorus. We found dative Ni–P bonds in every aspect of our analysis. These bonds were primarily covalent and showed a clear polarization between the more electronegative phosphorus and the electropositive nickel atom, as expected. Hence, we describe [Ni]P$_3$ as an *metallatetrahedrane* analogue. The shorter P–P bonds in [Ni]P$_3$ showed comparable or higher bond orders, but slightly less delocalization, than the longer P–P bonds in P$_4$. This was consistent with the reported reactivity of the air-stable [Ni]P$_3$ – especially when compared to the pyrophoric P$_4$.

Finally, this study clearly showed the advantages of a deeper insight into diffraction data supported by theoretical calculations, which can go far beyond a simple determination of the connectivity and geometry of a compound under investigation. It is evident that theoretical studies should much more often be carried out in concert with crystal structure determinations, rather than independently of them.

Supporting Information

The authors have cited additional references within the Supporting Information.[39–51] Deposition Number(s) ; 2300961 (for XRW-MoKa), 2300962 (for XRW-CuKb), 2300963 (for MM–MoKa), 2300838 (for MM–CuKb 2305139 (for HAR-MoKa), 2305140 (for HAR-CuKb), 2305141 (for NiP3_100 K), 2305142 (for NiP3_150 K), 2305143 (for NiP3_200 K), 2300862 (for NiP3_250 K) contain(s) the supplementary crystallographic data for this paper. These data are provided free of charge by the joint Cambridge Crystallographic Data Centre and Fachinformationszentrum Karlsruhe Access Structures service.

Conflict of Interests

The authors declare no conflict of interest.

Data Availability Statement

The data that support the findings of this study are available in the supplementary material of this article.

[1] A. Genoni, L. Bučinský, N. Claiser, J. Contreras-García, B. Dittrich, P. M. Dominiak, E. Espinosa, C. Gatti, P. Giannozzi, J. Gillet, D. Jayatilaka, P. Macchi, A. Ø. Madsen, L. Massa, C. F. Matta, K. M. Merz, P. N. H. Nakashima, H. Ott, U. Ryde, K. Schwarz, M. Sierka, S. Grabowsky, *Chem. Eur. J.* **2018**, *24*, 10881–10905.
[2] H.-B. Bürgi, A. Genoni, *Acta Crystallogr. Sect. B* **2022**, *78*, 298–304.
[3] D. Jayatilaka, *Phys. Rev. Lett.* **1998**, *80*, 798–801.
[4] E. S. Vosegaard, J. V. Ahlburg, L. Krause, B. B. Iversen, *Acta Crystallogr. Sect. B* **2023**, *79*, 380–391.
[5] E. Mädl, G. Balázs, E. V. Peresypkina, M. Scheer, *Angew. Chem.* **2016**, *128*, 7833–7838.
[6] C. Riesinger, L. Dütsch, G. Balázs, M. Bodensteiner, M. Scheer, *Chem. Eur. J.* **2020**, *26*, 17165–17170.
[7] R. Bianchi, G. Gervasio, D. Marabello, *C. R. Chim.* **2005**, *8*, 1392–1399.
[8] P. Macchi, D. M. Proserpio, A. Sironi, *J. Am. Chem. Soc.* **1998**, *120*, 13429–13435.
[9] A. Genoni, B. Meyer, *Adv. Quantum Chem.* **2016**, *73*, 333–362.
[10] M. Elian, M. M. L. Chen, D. M. P. Mingos, R. Hoffmann, *Inorg. Chem.* **1976**, *15*, 1148–1155.
[11] C. Jelsch, B. Guillot, A. Lagoutte, C. Lecomte, *J. Appl. Crystallogr.* **2005**, *38*, 38–54; N. K. Hansen, P. Coppens, *Acta Crystallogr. Sect. A* **1978**, *34*, 909–921.
[12] B. Guillot, L. Viry, R. Guillot, C. Lecomte, C. Jelsch, *J. Appl. Crystallogr.* **2001**, *34*, 214–223.
[13] N. K. Hansen, P. Coppens, *Acta Crystallogr. Sect. A* **1978**, *34*, 909–921.
[14] A. Ø. Madsen, *J. Appl. Crystallogr.* **2006**, *39*, 757–758.
[15] D. Jayatilaka, D. J. Grimwood, in *Computational Science – ICCS 2003*, Springer Berlin Heidelberg, Berlin, Heidelberg, **2003**, 142–151.
[16] S. C. Capelli, H.-B. Bürgi, B. Dittrich, S. Grabowsky, D. Jayatilaka, *IUCrJ* **2014**, *1*, 361–379.
[17] D. Jayatilaka, B. Dittrich, *Acta Crystallogr. Sect. A* **2008**, *64*, 383–393.
[18] F. Neese, F. Wennmohs, U. Becker, C. Riplinger, *J. Chem. Phys.* **2020**, *152*, 224108.
[19] F. Kleemiss, O. V. Dolomanov, M. Bodensteiner, N. Peyerimhoff, L. Midgley, L. J. Bourhis, A. Genoni, L. A. Malaspina, D. Jayatilaka, J. L. Spencer, F. White, B. Grundkötter-Stock, S. Steinhauer, D. Lentz, H. Puschmann, S. Grabowsky, *Chem. Sci.* **2021**, *12*, 1675–1692.
[20] O. V. Dolomanov, L. J. Bourhis, R. J. Gildea, J. A. K. Howard, H. Puschmann, *J. Appl. Crystallogr.* **2009**, *42*, 339–341.
[21] F. L. Hirshfeld, *Theor. Chim. Acta* **1977**, *44*, 129–138.
[22] F. D. Proft, R. Vivas-Reyes, A. Peeters, C. Van Alsenoy, P. Geerlings, *J. Comput. Chem.* **2003**, *24*, 463–470.
[23] E. Hupf, F. Kleemiss, T. Borrmann, R. Pal, J. M. Krzeszczakowska, M. Woińska, D. Jayatilaka, A. Genoni, S. Grabowsky, *J. Chem. Phys.* **2023**, *158*, 124103.
[24] M. Woińska, D. Jayatilaka, B. Dittrich, R. Flaig, P. Luger, K. Woźniak, P. M. Dominiak, S. Grabowsky, *ChemPhysChem* **2017**, *18*, 3334–3351.
[25] A. Simon, H. Borrmann, J. Horakh, *Chem. Ber.* **1997**, *130*, 1235–1240.
[26] V. Vukovic, PhD thesis, Université de Lorraine (France).
[27] R. F. W. Bader, *Atoms in Molecules: A Quantum Theory*, Clarendon Press; Oxford University Press, Oxford [England]: New York, **1994**.
[28] R. F. W. Bader, *Chem. Rev.* **1991**, *91*, 893–928.
[29] M. Haimerl, M. Piesch, G. Balázs, P. Mastrorilli, W. Kremer, M. Scheer, *Inorg. Chem.* **2021**, *60*, 5840–5850.
[30] A. T. Normand, E. D. S. Carrizo, C. Manoux, E. Lobato, H. Cattey, P. Richard, S. Brandès, C. H. Devillers, A. Romieu, P. Le Gendre, P. Fleurat-Lessard, *Chem. Sci.* **2021**, *12*, 253–269.

Chem. Eur. J. **2024**, e202303762 (7 of 8)

© 2024 The Authors. Chemistry - A European Journal published by Wiley-VCH GmbH

Chemistry–A European Journal

Research Article
doi.org/10.1002/chem.202303762

Chemistry Europe
European Chemical
Societies Publishing

[31] F. Spitzer, M. Sierka, M. Latronico, P. Mastrorilli, A. V. Virovets, M. Scheer, *Angew. Chem. Int. Ed.* **2015**, *54*, 4392–4396.

[32] M. Fugel, J. Beckmann, D. Jayatilaka, G. V. Gibbs, S. Grabowsky, *Chem. Eur. J.* **2018**, *24*, 6248–6261.

[33] a) J. S. Dewar, *Bull. Soc. Chim. Fr.* **1951**, *18*, C71; b) J. Chatt, L. A. Duncanson, *J. Chem. Soc.* **1953**, 2939–2947.

[34] R. Bianchi, C. Gatti, V. Adovasio, M. Nardelli, *Acta Crystallogr. Sect. B* **1996**, *52*, 471–478; G. T. Smith, P. R. Mallinson, C. S. Frampton, L. J. Farrugia, R. D. Peacock, J. A. K. Howard, *J. Am. Chem. Soc.* **1997**, *119*, 5028–5034.

[35] E. D. Glendening, C. R. Landis, F. Weinhold, *J. Comput. Chem.* **2019**, *40*, 2234–2241.

[36] I. G. Shenderovich, *Chem. Methods* **2021**, *1*, 61–70.

[37] I. G. Shenderovich, *J. Chem. Phys.* **2020**, *153*, 184501.

[38] I. G. Shenderovich, *Langmuir* **2020**, *36*, 11383–11392.

[39] *CrysAlisPro* (V.42) Rigaku Oxford Diffraction Ltd, **2019**.

[40] G. M. Sheldrick, *Acta Crystallogr. Sect. A* **2015**, *71*, 3–8.

[41] L. J. Bourhis, O. V. Dolomanov, R. J. Gildea, J. A. K. Howard, H. Puschmann, *Acta Crystallogr. Sect. A* **2015**, *71*, 59–75.

[42] K. Meindl, J. Henn, *Acta Crystallogr. Sect. A* **2008**, *64*, 404–418.

[43] B. Guillot, *Acta Crystallogr. Sect. A* **2012**, *68*, 204.

[44] J. C. Slater, *Phys. Rev.* **1951**, *81*, 385–390.

[45] C. Lee, W. Yang, R. G. Parr, *Phys. Rev. B* **1988**, *37*, 785–789.

[46] F. Weigend, R. Ahlrichs, *Phys. Chem. Chem. Phys.* **2005**, *7*, 3297.

[47] Y. Zhao, D. G. Truhlar, *Theor. Chem. Acc.* **2008**, *120*, 215–241.

[48] V. Bezugly, P. Wielgus, M. Kohout, F. R. Wagner, *J. Comput. Chem.* **2009**, *31*, 1504–1519.

[49] K. Alhameedi, G. S. Chandler, D. Jayatilaka, *Results in Chemistry* **2020**, *2*, 100053.

[50] T. Lu, F. Chen, *J. Comput. Chem.* **2012**, *33*, 580–592.

[51] F. Meurer, O. V. Dolomanov, C. Hennig, N. Peyerimhoff, F. Kleemiss, H. Puschmann, M. Bodensteiner, *IUCrJ* **2022**, *9*, 604–609.

[52] W. F. Kuhs, *Aust. J. Phys.* **1988**, *41*, 369–382.

[53] H. B. Bürgi, S. C. Capelli, H. Birkedal, *Acta Crystallogr. Sect. A* **2000**, *56*, 425–435.

[54] J. Schefer, D. Schwarzenbach, P. Fischer, Th. Koetzle, F. K. Larsen, S. Haussühl, M. Rüdlinger, G. McIntyre, H. Birkedal, H.-B. Bürgi, *Acta Crystallogr. Sect. B* **1998**, *54*, 121–128.

[55] *Gaussian*, M. J. Frisch, G. W. Trucks, G. E. Schlegel, G. E. Scuseris, M. A. Robb, J. R. Cheeseman, G. Scalmani, V. Barone, B. Mennucci, G. A. Petersson, H. Nakatsuji, M. Caricato, X. Li, H. P. Hratchian, A. F. Izmaylov, J. Bloino, G. Zheng, J. L. Sonnenberg, M. Hada, M. Ehara, K. Toyota, R. Fukuda, J. Hasegawa, M. Ishida, T. Nakajima, Y. Honda, O. Kitao, H. Nakai, T. Vreven, J. A. Montgomery, J. E. Peralta, F. Ogliaro, M. Bearpark, J. J. Heyd, E. Brothers, K. N. Kudin, V. N. Staroverov, T. Keith, R. Kobayashi, J. Normand, K. Raghavachari, A. Rendell, J. C. Burant, S. S. Iyengar, J. Tomasi, M. Cossi, N. Rega, J. M. Millam, M. Klene, J. E. Knox, J. B. Cross, V. Bakken, C. Adamo, J. Jaramillo, R. Gomperts, R. E. Stratmann, O. Yazyev, A. J. Austin, R. Cammi, C. Pomelli, W. Ochterski, R. L. Martin, K. Morokuma, V. G. Zakrzewski, G. A. Voth, P. Salvador, J. J. Dannenberg, S. Dapprich, A. D. Daniels, O. Farkas, J. B. Foresman, J. V. Ortiz, J. Cioslowski, D. J. Fox, **2013**.

[56] B. Zarychta, J. Zaleski, J. Kyziol, Z. Daszkiewicz, C. Jelsch, *Acta Crystallogr. Sect. B* **2011**, *67*, 250–262.

RESEARCH ARTICLE

F. Meurer, Prof. Dr. F. Kleemiss, Dr. C. Riesinger, Dr. G. Balázs, Dr. V. Vuković, Dr. I. G. Shenderovich, Dr. C. Jelsch, Dr. M. Bodensteiner*

1 – 9

Probing the Isolobal Relation between Cp′′′NiP$_3$ and White Phosphorus by Experimental Charge Density Analysis
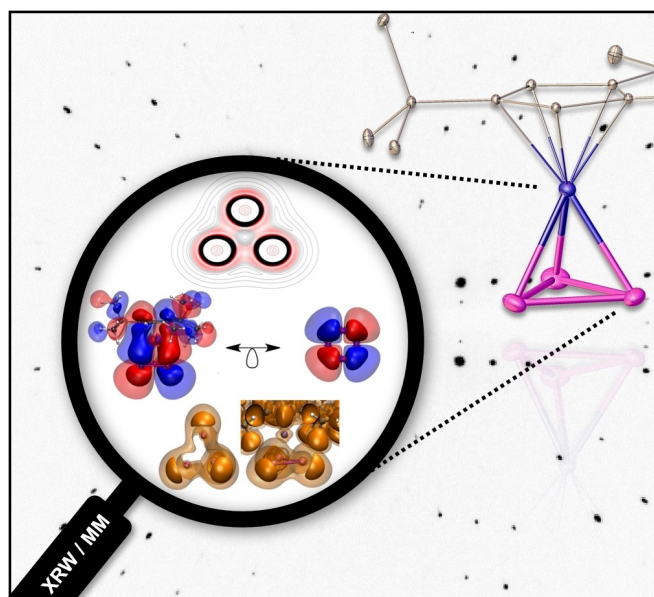
The isolobale principle as established by Hoffmann was tested in this work by the highest level of experimental charge density analysis. X-ray restrained wavefunction fitting as well as multipolar modelling showed in accord that [Ni]P$_3$ is a suitable isolobale analogue to white phosphorus. The deep dive into its bonding analysis reveals insights about the differences in reactivity compared to P$_4$.